

Dual Refinement Networks for Accurate and Fast Object Detection in Real-World Scenes

Xingyu Chen, Junzhi Yu, *Senior Member, IEEE*, Shihan Kong, Zhengxing Wu, and Li Wen *Member, IEEE*

Abstract—Object detection has been vigorously studied for years but fast accurate detection for real-world scenes remains a very challenging problem. Overcoming drawbacks of single-stage detectors, we take aim at precisely detecting objects for static and temporal scenes in real time. Firstly, as a dual refinement mechanism, a novel anchor-offset detection including an anchor refinement, a feature offset refinement, and a deformable detection head is designed for two-step regression and capture of accurate detection features. Based on the anchor-offset detection, a dual refinement network (DRN) is developed for high-performance static detection, where a multi-deformable head is further designed to leverage contextual information for describing objects. As for temporal detection in real-world scenes, temporal refinement networks (TRN) and temporal dual refinement networks (TDRN) are developed by propagating the refinement information across time, where we also propose a loose refinement strategy to match object motion with the previous refinement. Our proposed methods are evaluated on PASCAL VOC, COCO, and ImageNet VID datasets. Extensive comparison on static and temporal detection verify the superiority of DRN, TRN, and TDRN. Consequently, our developed approaches run in a fairly fast speed, and in the meantime achieve a significantly enhanced detection accuracy, i.e., a mAP of 82.8% on VOC 2007, 80.6% on VOC 2012, 69.4% on VID 2017, and an AP of 34.3% on COCO. Ultimately, producing encouraging results, our methods are applied to underwater object grasping with an autonomous system. Codes are publicly available at <https://github.com/SeanChenxy/TDRN>.

Index Terms—Object detection, neural networks, computer vision, deep learning.

I. INTRODUCTION

Object detection is one of the fundamental and challenging areas of research in computer vision, and with rapid advances in deep learning, convolutional neural networks (CNN) have demonstrated the state-of-the-art performance in this task. Zhao *et al.* presented an overview of modern object detection approaches [1]. From this review, we can see that two-stage detectors represented by RCNN family [2]–[4] and RFCN [5] usually attain an accurate yet slightly slow performance. On the contrary, by detecting objects in a one-step fashion,

This work was supported by the National Natural Science Foundation of China (nos. 61633004, 61633020, 61603388, and 61633017), and by the Beijing Natural Science Foundation (no. 4161002).

X. Chen, J. Yu, S. Kong, and Z. Wu are with the State Key Laboratory of Management and Control for Complex Systems, Institute of Automation, Chinese Academy of Sciences, Beijing 100190, China and University of Chinese Academy of Sciences, Beijing 100049, China. J. Yu is also with the Beijing Innovation Center for Engineering Science and Advanced Technology, Peking University, Beijing 100871, China {chenxingyu2015, junzhi.yu, kongshihan2016, zhengxing.wu}@ia.ac.cn

L. Wen is with the School of Mechanical Engineering and Automation, Beihang University, Beijing 100191, China, liwen@buaa.edu.cn

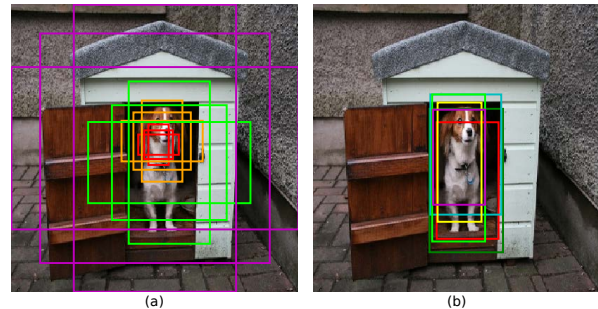


Fig. 1. Comparison of single-stage anchors and RPN outputs. For better visualization, only several key boxes are demonstrated. (a) Multi-scale SSD anchors; (b) RPN outputs in Faster RCNN.

single-stage detectors [6], [7] are able to run in real time with reasonably modest accuracy. Therefore, fast accurate detection remains a challenging problem for real-world applications.

It is heuristic that the two-stage method is adept at high accuracy while the single-stage detector has a desirable inference speed, so this inspires us to investigate the reasons. In our opinion, the high accuracy of two-stage approaches comes with two advantages: i) two-step regression and ii) relatively accurate features for detection. In detail, two-stage detectors firstly regress pre-defined anchors with the aid of region proposal [2], and this operation significantly eases the difficulty of final localization. Besides, an RoI-wise subnetwork [4] is appended to the region proposal part, so features in pre-regressed boxes can be leveraged for final detection. By contrast, there are two drawbacks in the single-stage paradigm: i) detection head directly regresses coordinates from anchors, but most anchors are far from matching object regions; ii) classification information comes from probably inaccurate locations, where features could not be precise enough to cover objects. Referring to Fig. 1(a), it is relatively difficult to regress pre-defined anchors to precisely surround the object (e.g., the dog in Fig. 1). Moreover, as feature sampling locations for describing object follow pre-defined anchor regions, detection features for small-scale anchors cannot cover the entire object region while that for large-scale anchors weaken the object because of background. On the contrary, the two-stage methods with region proposal detect the dog with a better initialization (see Fig. 1(b)). Thus, the strengths of two-stage methods exactly reflect the single-stage drawbacks that lead to relatively lower detection accuracy. Although Zhang *et al.* developed RefineDet [8] to introduce two-step regression to the single-stage detector, it still failed to capture accurate detection

features, i.e., pre-defined feature sampling locations are not precise enough for describing refined anchor regions. (Note that detailed comparison between RefineDet and our approach will be presented in III-B.) Thus, there is an imperative need of further overcoming these single-stage limitations for real-time accurate object detection.

In addition, most researches have largely focused on detecting object statically, ignoring temporal coherence in real-world applications. Detection in real-world scenes was introduced by ImageNet video detection (VID) dataset [9]. To the best of our knowledge, main ideas of temporal detection include i) post processing [10], ii) tracking-based location [11], [12], iii) feature aggregation with motion information [11], [13]–[16], iv) RNN-based feature propagation [15], [17]–[19], and v) batch-frame processing (i.e., tubelets proposal) [20]. All these ideas are attractive in that they are able to leverage temporal information for detection, but they also have respective limitations. In brief, methods i)–iv) borrow other tools (e.g., tracker, optical flow, LSTM, etc.) for temporal analysis; methods iii) and iv) focus on constructing superior temporal features but still detect objects following the static mode; method v) works in a non-causal offline mode that prohibits these methods from real-world tasks. Furthermore, most recent works pay excessive attention to accuracy so that high computational costs could affect time efficiency. Thus, a novel temporal detection mode should be developed for real-world tasks.

Overcoming aforementioned single-stage drawbacks, a dual refinement mechanism is proposed in this paper for static and temporal visual detection, namely anchor-offset detection, where an anchor refinement and a feature offset refinement are developed for two-step regression and capture of accurate single-stage features for detection. Besides, a deformable detection head is designed to leverage this dual refinement information. Based on the anchor-offset detection, a dual refinement network (DRN), temporal refinement networks (TRN), and temporal dual refinement networks (TDRN) are proposed for the purpose of real-time accurate object detection in real-world scenes. Besides, DRN is equipped with a multi-deformable head for diversifying detection receptive fields for more contextual information, whereas TRN and TDRN are composed of a reference generator and a refinement detector with the aim of propagating refinement information across time. Additionally, we propose a loose refinement strategy for TRN to match object motion with previous refinement information. Our proposed DRN, TRN, and TDRN are validated on PASCAL VOC [21], COCO [22], and ImageNet VID [9] datasets. As a result, our methods achieve a real-time inference speed and considerably improved detection accuracy. Furthermore, these approaches have been applied to object-driven navigation and grasping in an unstructured undersea environment. Our contributions are summarized as follows:

- Starting with drawbacks of single-stage detectors, an anchor-offset detection including an anchor refinement, a feature-offset refinement, and a deformable detection head is proposed for two-step regression and capture of accurate single-stage detection features. A DRN based on the anchor-offset detection and a multi-deformable head is developed to elevate static detection accuracy while

maintaining real-time inference speed.

- Without the aid of any other temporal modules, a TRN and a TDRN are proposed based on the anchor-offset detection for temporal vision. They are characterized by a better accuracy vs. speed trade-off and concise training process without the requirement of sequential data.
- The single-stage DRN maintains fast speed while acquiring significant improvements in accuracy, i.e., 82.8% mean average precision (mAP) on VOC 2007 test set, 80.6% mAP on VOC 2012 test set, and 34.3% AP on COCO test-dev2015. Based on VID 2017 validation set, DRN sees 69.4% mAP; TRN achieves 66.5% mAP; and TDRN obtains 67.3% mAP.
- With an aquatic autonomous system, our methods are applied to underwater object grasping, and the results are quite promising.

The remainder of this paper is organized as follows. Section II presents the related works. DRN including anchor-offset detection and multi-deformable head is elaborated in Section III. The Section IV presents TRN and TDRN in detail, and the Section V provides the experimental results and discussion. Conclusion are summarized in Section VI.

II. RELATED WORK

A. CNN-based Static Object Detection

Deep learning methods including two-stage approaches and single-stage detectors have recently dominated the field of object detection [1]. Two-stage detectors [2]–[5], [23]–[27] usually detect objects by region proposal, location, and classification. For example, inspired by Faster RCNN [4] and RFCN [5], CoupleNet [23] leveraged both region-level and part-level features to express a variety of object challenging situations, which achieved considerable detection accuracy but it just ran at 8.2 FPS. As groundbreaking works, YOLO [6] and SSD [7] directly locate and classify objects from pre-defined anchors using a single-shot network for real-time detection. Recently, many revised single-stage versions have emerged [8], [29]–[34]. Typically, in favor of small object detection, Lin *et al.* developed a RetinaNet to formulate the single-shot network as an FPN [28] fashion for propagating information in a top-down manner to enlarge shallow layers' receptive field [29]. Zhang *et al.* designed a RefineDet to introduce two-step regression to single-stage pipeline [8]. RefineDet first adjusted pre-defined anchors for more precise localization but its detection features still fixed on pre-defined positions, failing to precisely describe refined anchor regions. In short, although the single-stage methods has a superiority in speed, the two-stage methods still dominates the detection accuracy on generic benchmarks [9], [21], [22]. Hence, this motivates us to analyze single-stage drawbacks from two-stage merits (analyzed in Section I), and construct DRN with both competitive detection accuracy and fast inference speed.

B. Temporal Object Detection

To detect objects in temporal vision, some post-processing methods have been first investigated to merge multi-frame

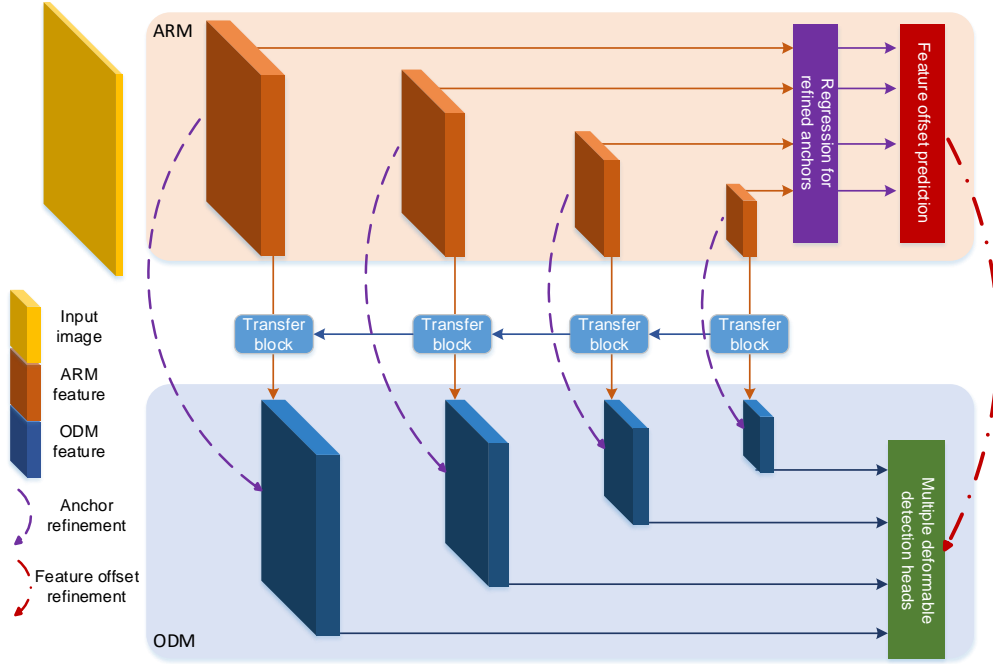


Fig. 2. The schematic layout of the proposed DRN. Refined anchors are produced by coarse regression with ARM features, and they are first employed to predict feature offsets, namely, feature offset refinement. The detection head utilizes ODM feature maps, refined anchors, and refined feature sampling locations to detect objects, i.e., anchor-offset detection. A multi-deformable head is designed for rich contextual information.

results, then tracker-based detection, motion-guided feature aggregation, RNN-based feature integration, and tubelet proposal are studied by the research community. Han *et al.* proposed an SeqNMS to discarded temporally interrupted bounding boxes in the non-maximum suppression (NMS) phrase [10]; Feichtenhofer *et al.* combined RFCN and a correlation-filter-based tracker to boost recall rate [12]. Based on motion estimation with optical flow, Zhu *et al.* devised a temporally-adaptive key frame scheduling to effective feature aggregation [14]; Chen *et al.* and Liu *et al.* took advantage of Long Short-Term Memory to propagate CNN features across time [18], [19]. However, the temporal analysis capacity in above-mentioned methods borrowed from other temporal tools, and some methods focused on how to constructed superior temporal features but still remained possibly improper static detection mode. As a typical offline detection mode, Kang *et al.* reported a TPN to propose tubelets (i.e., temporally propagated boxes) instead of boxes, so TPN could simultaneously process multiple frames to elevate temporal stability [20]. However, the batch-frame mode struggled to be qualified for real-world tasks. On the contrary, without the aid of any other temporal tools, we developed a real-time online detection mode for videos using the idea of refinement. That is, refined anchors and refined feature sampling locations are generated with key frames, which will be temporally propagated for detection. Moreover, compared to most video detectors, our methods have a concise training process without the need for sequential images.

C. Sampling for Detection

It is widely accepted that spatial sampling is important to construct robust features. For example, Peng *et al.* detected

objects by an improved multi-stage particle window that can sample a small number of key features for detection while maintaining high accuracy [35]. In terms of CNN, canonical convolution is based on a square kernel that is not suited enough to variform objects. For augmenting the spatial sampling locations, Dai *et al.* proposed deformable convolutional networks to combat fixed geometric structures in traditional convolution operation, and the deformable convolution significantly boosts the detection accuracy of RFCN [36]. As for video detection, Bertasius *et al.* used the deformable convolutions across time and constructed robust features for temporally describing objects [16]. In this paper, we tend to capture accurate single-stage features for detection, and more specifically, refined feature locations are sampled based on refined anchors.

III. DUAL REFINEMENT NETWORK

In this section, the proposed DRN will be presented. The network architecture is first briefed, then, we will demonstrate how to overcome two key single-stage drawbacks with anchor-offset detection. Next, our designed multi-deformable head is delineated, followed by the training and inference.

A. Overall Architecture

1) *Basic Structure:* As shown in Fig. 2, our proposed architecture is a single-shot network with a forward backbone (e.g., VGG16 [39]) for feature extraction. The network generates a fixed number of bounding boxes and corresponding classification scores, followed by the NMS for duplicate removal. Inheriting from RefineDet [8], there is an anchor refinement module (ARM) and an object detection module (ODM) for

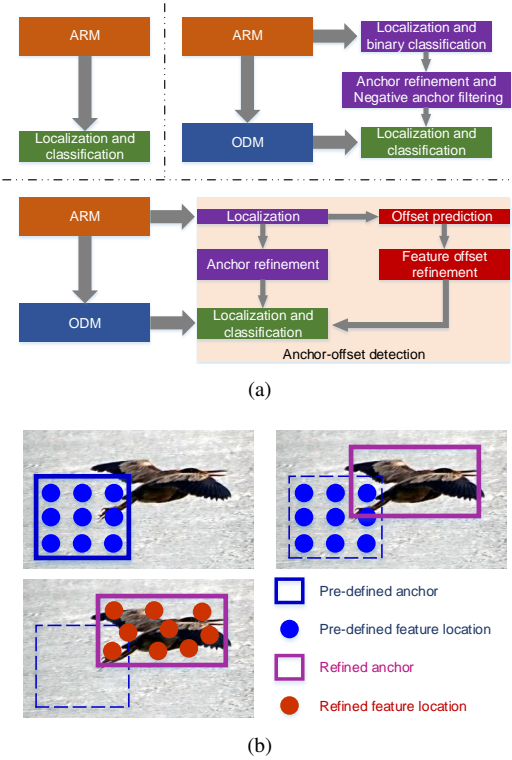


Fig. 3. Comparison of three single-stage detectors. (a) Structure sketch of SSD (left, top), RefineDet (right, top), and DRN (bottom); (b) Detection modes of SSD (left, top), RefineDet (right, top), and DRN (left, bottom). (b) shows the main idea of the anchor-offset detection.

two-step regression. ARM regresses coordinates for refined anchors, then feature offsets are predicted using the refined anchors. In ODM, a creative detection head is designed with deformable convolution for final classification and regression, whose inputs are ODM features, refined anchors, and feature offsets. Furthermore, a multi-deformable head is developed with multiple detection paths to leverage contextual information for detection.

B. Anchor-Offset Detection

1) *From SSD to RefineDet, then to DRN*: As illustrated in Fig. 3(a), SSD directly detects objects with ARM features, whereas RefineDet adopts FPN for strong semantic information. Moreover, RefineDet develops an anchor refinement for more precision localization and a negative anchor filtering for addressing extreme class imbalance problem. In our DRN, we inherit anchor refinement but discard the negative anchor filtering since training with hard negative mining [7] induces a similar effect. More specifically, a feature offset refinement and a deformable detection head are proposed to combat another key drawback in the single-stage paradigm, i.e., inaccurate feature sampling locations.

In general, detection in traditional SSD-like manner is based on hand-crafted anchors which are rigid and usually inaccurate. Pre-defined anchors and fixed feature locations could not be suited enough to regress and classify objects (see the left top in Fig. 3(b)). Through preliminary localization, refined anchors in RefineDet are in favor of more precise

coordinate prediction. However, RefineDet still uses inaccurate feature sampling locations (see the right top in Fig. 3(b)) for regression and classification. Overcoming these difficulties, our designed anchor-offset detection is able to achieve two-step regression and capture more accurate detection features (see the left bottom in Fig. 3(b)).

2) *Anchor Refinement*: This process is analogous in essence to RefineDet, i.e., using ARM to generate refined anchors that provide better initialization for the second-step regression. A location head generates refined anchors ar using ARM features f_{ARM} with convolution operation. That is, $ar = W_{ar} * f_{ARM}$, where $*$ denotes convolution (W is the convolutional weight). Note that ar is the coordinate offset from original anchors.

3) *Deformable Detection Head*: According to deformable convolution [36], a deformable detection head is designed to leverage the refinement information. The standard detection head in SSD uses a regular 3×3 grid \mathcal{R} to predict category probability and coordinates for a feature map cell. In the meantime, through careful anchor design, the respective field of \mathcal{R} can describe a specific anchor region. Thus, the prediction can be given as $P_{p_0} = \sum_{p \in \mathcal{R}} w(p) \cdot f_{ODM}(p)$, where P is the prediction of category probability or coordinate offset; w is the convolution weight; p_n represents positions in \mathcal{R} while p_0 is the center; f_{ODM} denotes ODM features.

However, the respective field of \mathcal{R} usually fails to describe the refined anchor region (see the right top of Fig. 3(b)). Thereby, allowing \mathcal{R} to deform to fit various anchor changes, the deformable detection head is developed to capture accurate features with the feature offset δp ,

$$P_{p_0} = \sum_{p \in \mathcal{R}} w(p) \cdot f_{ODM}(p + \delta p). \quad (1)$$

The bilinear interpolation allows δp to be a fraction.

4) *Feature Offset Refinement*: The offset $\Delta p = \{\delta p\}$ is computed with the input feature in original deform pipeline,

$$\Delta p = W_{fr} * f_{ODM}. \quad (2)$$

Nevertheless, there is a strong demand for describing the refined anchor regions with the deformed grids. Therefore, our feature offsets are predicted based on refined anchors, i.e., feature offset refinement,

$$\Delta p = W_{fr} * ar. \quad (3)$$

In detail, this operation is a convolution with 1×1 kernel. Since each spatial element in ar is coordinate offsets for refined anchors, its channel information is fused for feature offset refinement.

In this way, the refined feature locations can describe refined anchor regions more effectively. We call this detection mode anchor-offset detection, which can be formulated as

$$\begin{aligned} P_{local} &= (W_{local} * (f_{ODM}, \Delta p)) \oplus (ar \oplus ao) \\ P_{class} &= W_{conf} * (f_{ODM}, \Delta p). \end{aligned} \quad (4)$$

where \oplus, ao represent anchor decoding operation [7] and the original anchor, respectively; $W * (f, \Delta p)$ denotes deformable convolution. As ar is the coordinate offset from ao , $ar \oplus ao$ is the refined anchor. The operation of two \oplus is two-step

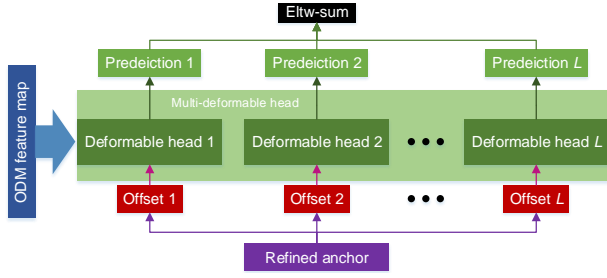


Fig. 4. Multi-deformable head. It is designed with different detection respective field. Multiple detection paths are induced, where feature offset refinement is independent for each path. Their results are fused using summation.

regression that elevates the precision of localization, while Δp is the feature offset that constructs the accurate single-stage detection features.

C. Multi-Deformable Head

CoupleNet developed local and global FCN to detect objects [23]. The local FCN focused local features in a region proposal while the global one paid attention to the whole region-level features. In this way, more semantic information and underlying object relation are exploited for high-quality detection. Thus, taking aim at describing the object using original, shrunken, and expansile region-level features, a multi-deformable head is developed for the single-stage detector. The shrunken region-level features are in favor of leveraging local messages while the expansile region-level features contain more contextual information and object relation.

In this way, multiple detection head is designed with different respective field sizes, inducing multiple detection paths. As shown in Fig. 4, each of detection path is an anchor-offset detection, and their feature offset refinement is independent. In addition, their results are fused with element-wise summation. The detection based on L deformable heads can be given as:

$$\begin{aligned} P_{local} &= (\sum_{l=1}^L W_{local_l} * (f_{ODM}, \Delta p_l)) \oplus (ar \oplus ao) \\ P_{class} &= \sum_{l=1}^L W_{conf_l} * (f_{ODM}, \Delta p_l), \end{aligned} \quad (5)$$

D. Training and Inference

During training, the pre-trained VGG16 model on ImageNet [9] are employed, and L2 normalization is used to scale norms of $Conv4_3, Conv5_3$ to 10 and 8, respectively. As for pre-defined anchor setting, each feature layer is associated with one specific scale of anchors. In detail, the anchor size of [32, 64, 128, 256] is adopted for 4-scale feature maps from low-level to high-level, and 3 anchors are tiled at each feature map cell with aspect ratios of [1.0, 2.0, 0.5]. In terms of optimization, an SGD optimizer with 0.9 momentum and 0.0005 weight decay is employed to train the whole network.

A multi-task objective is designed to train DRN including two localization losses $\mathcal{L}_{loc-arm}, \mathcal{L}_{loc-odm}$ and a confidence loss \mathcal{L}_{conf} , i.e., $\mathcal{L} = \frac{1}{N_{ARM}} \mathcal{L}_{loc-ARM} + \frac{1}{N_{ODM}} (\mathcal{L}_{loc-ODM} + \mathcal{L}_{conf})$, where N is the number of positive boxes in ARM and ODM. $\mathcal{L}_{loc} = \sum_{i=1}^N sommothL1(p_i - g_i^*)$, where g_i^* is the ground truth coordinates of the i -th positive anchor.

Before computation of \mathcal{L}_{loc} , anchors should be determined to be positive or negative based on jaccard overlap [7]. We handle original anchors and refined anchors for $\mathcal{L}_{loc-ARM}$ and $\mathcal{L}_{loc-ODM}$, respectively, by the following processes. Firstly, each ground truth box is matched to anchors with the best jaccard overlap, then anchors with > 0.5 overlap will be matched to corresponding ground truth box. Let c_i^{cls} be the probability that the i -th predicted box belongs to class cls ($cls = 0$ for background). $\mathcal{L}_{conf} = -\sum_{i=1}^N \log(c_i^{cls}) - \sum_{i=1}^{\delta N} \log(c_k^0)$, where δN negative anchors are selected by hard negative mining [7]. This operation selects a part of negative boxes with top loss values for training to address the problem with extreme foreground-background class imbalance, and $\delta = 3$.

In the phase of inference, the anchor-offset detection predicts confident object candidates (confident scores > 0.01) in the manner of anchor-offset detection and multi-deformable head. Subsequently, these candidates are processed by NMS with 0.45 jaccard overlap pre class and retain top 200 high confident objects as the final detections.

IV. TEMPORAL DUAL REFINEMENT NETWORKS

In this section, we present how to propagate refined anchors and refined feature sampling locations across time, and construct TRN and TDRN.

A. Architecture

A reference generator (RG) and a refinement detector (RD) are designed in this section, both of which are constructed with the same structure, i.e., canonical SSD framework [7] with 4-scale detection features (see Fig. 5(a)). Like ARM in DRN, RG predicts refinement information including refined anchors or both refine anchors and feature offsets. Similar to ODM in DRN, RD takes over RG's outputs as references, and detect objects frame by frame. If RG only predicts refined anchors, the framework is called TRN. When feature offsets are also involved, the anchor-offset detection with a deformable detection head is also employed by RD, and we call this structure TDRN.

B. Training

In general, temporal detectors usually have a complex training process with sequential images. For example, TSSD developed a multi-step training strategy [19], and the initialization for multi-frame regression layer in TPN is complicated [20]. Conversely, the training process for TRN and TDRN is refreshingly concise, and it also eliminates the need of sequential training images. As shown in Fig. 5(b), during the training process, RG and RD play similar roles to DRN's ARM and ODM, respectively. Thereby, both RG and RD can be trained with static images following DRN's basic training settings and loss functions.

C. Inference

Consider a video as an image sequence, i.e., $V = \{I_0, I_1, \dots, I_M\}$. TRN and TDRN attempt to obtain frame-level detections $\{D_0, D_1, \dots, D_M\}$, where D_m contains the boxes

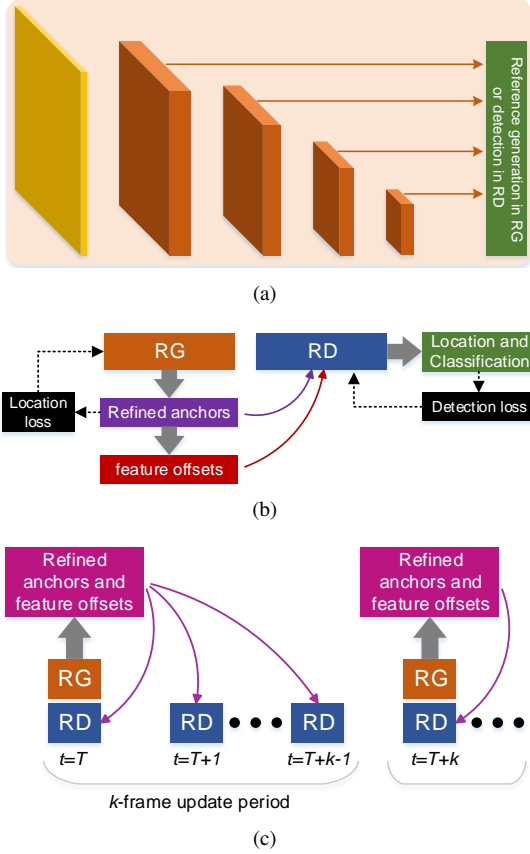


Fig. 5. Designs of the proposed TDRN. (a) Basic network structure for RG and RD (a) The training phase; (b) The testing phase.

and class predictions of I_m . RG takes over I_m and outputs refined anchor ar and feature offset Δp ,

$$ar_m, \Delta p_m = RG(I_m). \quad (6)$$

Then, RD detect objects with I_m , ar , and Δp ,

$$D_m = RD(I_m, ar, \Delta p) = \begin{cases} (W_{local} * (f_{I_m}, \Delta p)) \oplus (ar \oplus ao) \\ W_{conf} * (f_{I_m}, \Delta p), \end{cases} \quad (7)$$

where f_{I_m} is the feature extracted from I_m .

Despite the similar detection mode, it is apparent that RD is more computationally efficient than DRN. Therefore, considering the temporal context in temporal vision, a key frame duration is used for RG to pursue a better trade-off between accuracy and speed. That is, only key frames will be processed by RG while non-key frames are just detected by RD with previous RG's outputs. Mathematically, in (7), $ar = ar_m, \Delta p = \Delta p_m$ for key frames, whereas for non-key frames, $ar, \Delta p$ are from the previous key frame. In this manner, ar and Δp are propagated as the temporal information. As illustrated in Fig. 5(c), RG generates refinement references using the first periodic frame that will survive k time stamps, and RD detects objects based on these references in the whole period. It is apparent that frequent reference update would lead to higher detection accuracy and more computational costs, so the trade-off between accuracy and speed can be adjusted by different k setting.

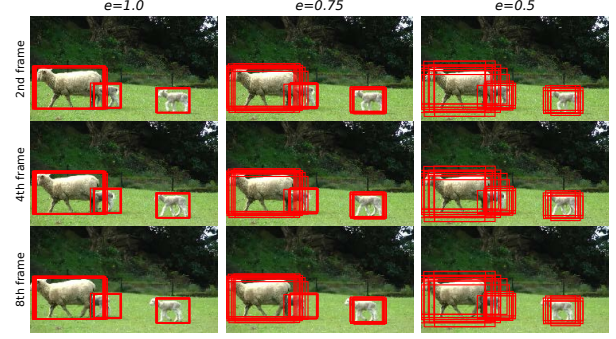


Fig. 6. Loose refinement strategy. To match object motion with the previous refinement, a loose factor e is introduced to TRN. For better visualization, only key refined anchors are demonstrated.

Taking aim at adapting to various object motion, a loose refinement strategy is proposed with a loss factor e . In SSD, the intent of designing anchor is to use numerous boxes to cover the whole image as the prior knowledge, but significantly discarding anchor diversity, the refined anchors tend to surround foreground. It is known that refined anchors are in favor of static detection, but objects in videos have a variety of motion properties or pose changes. Hence, the loose refinement strategy is designed to retain the anchor diversity for relatively long temporal detection period. The loose refinement operation can be given as $ar_l = ar \times e$, where ar_l is the loose refined anchor, and as a scalar, $e \in [0, 1]$ multiplies each element in a tensor. As ar is the offset from original anchors, $ar \times e$ can loose intensity of refinement. Referring to Fig. 6, refined anchors are computed by the first frame in the period, then some key refined anchors are visualized in the 2nd, 4th, and 8th frames. Without the loose refinement strategy, they gradually fail to be precisely aware of objects across time. For example, when $e = 1$, refined anchors cannot surround the head of a sheep in the 8th frame. This phenomenon causes regression difficulties for RD, and prohibits k from increasing. That is, $e = 1$ incur that the refinement information can hardly be propagated in a relatively long range of time series. When $e = 0.75$ or 0.5 , this drawback is mitigated so that an update period can be longer for a better trade-off between accuracy and speed.

V. EXPERIMENTS AND DISCUSSIONS

Our methods are implemented under the PyTorch framework. The training and experiments are carried out on a workstation with an Intel 2.20 GHz Xeon(R) E5-2630 CPU, NVIDIA TITAN-1080 GPUs, CUDA 8.0, and cuDNN v7. Without any extra test tricks, our approaches are trained and evaluated on PASCAL VOC [21], COCO [22], and ImageNet VID [9] datasets. Furthermore, we applied TDRN to underwater object grasping based on an aquatic autonomous system.

A. Ablation Studies of DRN320-VGG16 on VOC 2007

Experiments on PASCAL VOC 2007 are first conducted to study the proposed dual refinement mechanism in detail. In this section, the models are trained on the union set of VOC



Fig. 7. Visualization of refined feature sampling locations for *Conv5_3*. For better visualization, only the sampling centers (i.e., the center dot in left-bottom Fig 3(b)) are demonstrated. The original sampling centers are illustrated with green dots, which are regularly tiled on images. The red dots show the refined sampling centers that have a stronger capability of describing objects. These images are from VOC, COCO and ImageNet VID.

TABLE I
Ablation Studies of DRN320 on VOC 2007. THE BASELINE IS 79.1%

Component		DRN320-VGG16				
multi-deformable head?				✓		✓
feature offset refinement?		✓	✓		✓	✓
deformable detection head?	✓	✓	✓		✓	✓
BN for VGG&extra?				✓	✓	✓
mAP(%)	78.3	79.8	80.5	81.1	81.7	82.0

TABLE II
Effectiveness of various multi-deformable head designs. A VARIETY OF DETECTION PATHS WITH DIFFERENT CONVOLUTIONAL KERNEL SIZE (ks) AND DILATION (di) ARE USED TO VALIDATE THE EFFICACY OUR DESIGNS.

$ks = 5 \times 5, di = 1?$				✓	✓
$ks = 3 \times 3, di = 2?$			✓		
$ks = 1 \times 1, di = 1?$		✓	✓	✓	
$ks = 3 \times 3, di = 1?$	✓	✓	✓	✓	✓
mAP(%)	79.8	79.8	79.4	80.5	80.3

2007 trainval and VOC 2012 trainval (16, 551 images, denoted as “07+12”), and evaluated on VOC 2007 test set (4, 952 images). We use mAP to describe the detection accuracy. For the convenience of comparison, RefineDet without negative anchor filtering is employed as the baseline, whose mAP is 79.1% in our re-produced PyTorch implementation (Note that it is 79.5% in original Caffe implementation). The changes of mAP caused by various model designs are shown in Table I.

1) *Anchor-Offset Detection*: The anchor-offset detection contains an anchor refinement, a feature offset refinement, and a deformable detection head, the first of which has been studied by [8], so we focus on the latter two components. At first, the deformable detection head without feature offset refinement is tested. Following [36], the offsets are computed with ODM features (referring to (2)). As a result, this change leads to 0.8% mAP drop. In our opinion, this should be attributed to improper offsets. That is, the refined anchors are computed with ARM while the feature offsets are from ODM, so they are independent, making refined features still fail to describe refined anchor regions.

The refined anchors have been displayed in Fig. 6, so the refined feature sampling locations are also demonstrated in Fig. 7 to better explain the advantages of the proposed anchor-offset detection. For better visualization, only the sampling centers (i.e., the center dot in left-bottom Fig. 3(b)) are demonstrated. Referring to green dots in Fig. 7, the pre-defined detection features are regularly fixed on feature maps (their locations are mapped to the original images for visualization). This design is justified for the traditional SSD since anchors

are also tiled in the same manner. However, the refined anchors tend to surround objects for more precision localization (see Fig. 6), so it is reasonable that the feature locations should have the same tendency. As shown with red dots, gathering towards objects, the refined feature locations are more suitable for regression and classification. Moreover, in some areas away from objects, the refined feature locations would not blindly shift towards targets so that the detection capability for the whole image can be maintained.

Therefore, the operation of the proposed feature offset refinement is crucial to capture accurate detection features. Following the pipeline of anchor-offset detection, the refined feature locations are tightly associated with refined anchors. Thus, a 0.7% mAP rise (i.e., 79.8% vs. 79.1%) is induced.

2) *Multi-Deformable Head*: For leveraging more contextual information for detection, multiple detection paths are devised with various respective field sizes, or convolution kernel size and dilation. The effectiveness of various multi-deformable designs is shown in Table II. At first, the 1×1 grid is employed to utilize shrunken region-level features, but it incurs negligible effectiveness. The 1×1 grid should have focused on most suitable local parts for detection, but feature offsets are computed with refined anchors in our pipeline, ignoring suitable local parts. Then, the 3×3 grid with dilation is devised as one of the detection paths, but it leads to 0.4% drop in mAP. Although it expands the respective field, the dilated 3×3 grid splits features and fails to describe objects effectively. To cover the shortage, the 5×5 grid without dilation could work more effectively, and experimentally, it invites 0.7% rise in mAP

TABLE III

Results on Pascal VOC 2007 and 2012 test dataset. “TRAIN DATA” IS USED FOR VOC 2007 TRAINING, AND THAT OF VOC 2012 CONTAINS AN EXTRA VOC 2007 TEST SET. “S” DENOTES INSTANCE SEGMENTATION LABELS.. WE ONLY LIST THE RESULTS WITHOUT ANY TESTING TRICKS. BOLD FONTS INDICATE THE BEST SINGLE-STAGE RESULTS.

Method	Backbone	Tran data	Input size	#Boxes	FPS	mAP(%)	
						VOC 2007	VOC 2012
<i>two-stage</i>							
Fast RCNN [3]	VGG16	07+12	1000 × 600	~ 2000	0.5	70.0	68.4
Faster RCNN [4]	VGG16	07+12	1000 × 600	300	7	73.2	70.4
OHEM [27]	VGG16	07+12	1000 × 600	300	7	74.6	71.9
HyperNet [25]	VGG16	07+12	1000 × 600	100	0.9	76.3	71.4
ION [26]	VGG16	07+12+S	1000 × 600	4000	1.3	76.5	76.4
Faster RCNN [4]	ResNet101	07+12	1000 × 600	300	2.4	76.4	73.8
R-FCN [5]	ResNet101	07+12	1000 × 600	300	9	80.5	77.6
CoupleNet [23]	ResNet101	07+12	1000 × 600	300	8.2	82.7	80.4
Attention CoupleNet [24]	ResNet101	07+12+S	1000 × 600	300	6.9	83.1	81.0
<i>single-stage</i>							
YOLO [6]	GoogleNet [40]	07+12	448 × 448	98	45.0	63.4	57.9
RON384 [32]	VGG16	07+12	384 × 384	30600	15.0	75.4	73.0
SSD321 [30]	ResNet101	07+12	321 × 321	17080	11.2	77.1	75.4
SSD300 [7]	VGG16	07+12	300 × 300	8732	90.0*	77.2	75.8
DSOD300 [34]	DenseNet [43]	07+12	300 × 300	8732	17.4	77.7	76.3
YOLOv2 [31]	Darknet19	07+12	544 × 544	1445	40.0	78.6	73.4
DSSD321 [30]	ResNet101	07+12	321 × 321	17080	9.5	78.6	76.3
SSD512 [7]	VGG16	07+12	512 × 512	24564	19.0	79.8	78.5
RefineDet320 [8]	VGG16	07+12	320 × 320	6375	60.0*	80.0	78.1
RFBNet300 [33]	VGG16	07+12	300 × 300	8808	83.0*	80.5	-
SSD513 [30]	ResNet101	07+12	513 × 513	43688	6.8	80.6	79.4
DSSD513 [30]	ResNet101	07+12	513 × 513	43688	5.5	81.5	80.0
RefineDet512 [8]	VGG16	07+12	512 × 512	16320	24.1	81.8	80.1
RFBNet512 [33]	VGG16	07+12	512 × 512	24692	38.0*	82.2	-
DRN320	VGG16	07+12	320 × 320	6375	55.2*	82.0	79.3 [†]
DRN512	VGG16	07+12	512 × 512	16320	32.2*	82.8	80.6[‡]

*: Pytorch speed. †: <http://host.robots.ox.ac.uk:8080/anonymous/18COCB.html> ‡: <http://host.robots.ox.ac.uk:8080/anonymous/V1DWET.html>

(i.e., 80.5% vs. 79.8%) since more contextual information is involved. In addition, the 1×1 detection path is removed and this more efficient design still can reach 80.3% in mAP. We adopt this design for subsequent experiments. In addition, this series of comparisons also indicates that the improvement of multi-deformable head comes from above-analyzed reasons rather than increasing parameter size.

3) *Towards More Effective Training*: BN is an effective approach that solves vanishing and exploding gradient problem [38], so this tactic is introduced to the feature extractor (i.e., the VGG16 and extra layer) for more effective training. Then, a significant improvement in accuracy is incurred, i.e., 81.1% mAP. Subsequently, the anchor-offset detection and multi-deformable head further boost the performance. Referring to Table I, removing the multi-deformable head leads to 0.3% drop in mAP, and removing the anchor-offset detection invites another 0.6% mAP drop. Thus, our designs are still efficient, making the state-of-the-art detection performance with such a small input image, i.e., 82.0% mAP and 320×320 input size.

B. Results on VOC 2007

With VGG16 as the backbone, we use the initial learning rate of 0.001 for the first 130 training epochs, then use the

learning rate of 0.0001 for the next 40 epochs and 0.00001 for another 40 epochs. Referring to Table III, our DRN320 achieves 82.0% mAP without bells and whistles, which surpasses all methods with such small inputs by a large margin. When compared to SSD300, our method outperforms it by 4.8 points (i.e., 82.0% vs. 77.2%), and DRN320 further improves mAP by 2.0% as for RefineDet320 (i.e., 82.0% vs. 80.0%). When compared to RFBNet300, our DRN320 also has 1.5-point higher mAP (i.e., 82.0% vs. 80.5%).

For 512×512 input size, DRN obtains 82.8% mAP that is also competitive with all compared methods. Only Attention CoupleNet [24] has slightly higher mAP than ours (i.e., 82.8% vs. 83.1%). However, Attention CoupleNet uses ResNet101 [41] as its backbone, and its results come with larger input size (i.e., 1000×600). Besides, Attention CoupleNet introduces extra segmentation annotations to its multi-scale training processing. In addition, DRN512’s inference speed surpasses that of Attention CoupleNet by a large margin (i.e., 32.2 vs. 6.9 FPS). Therefore, the proposed DRN achieves a better trade-off between accuracy and speed.

C. Results on VOC 2012

More challenging VOC 2012 dataset is employed to evaluate our proposed designs, and we use the union set of VOC 2007

TABLE IV

Results on COCO 2015 test-dev. “AP” IS EVALUATED AT IOU THRESHOLDS FROM 0.5 TO 0.95. “AP@0.5”: PASCAL-TYPE METRIC, IOU= 0.5. “AP@0.75”: EVALUATED AT IOU= 0.75. AP_S , AP_M , AP_L : AP AT DIFFERENT SCALES. WE ONLY LIST THE RESULTS WITHOUT ANY TESTING TRICKS. BOLD FONTS INDICATE THAT WE DRAW READERS’ ATTENTION TO A DEEP COMPARISON.

Method	Backbone	Tran data	AP	AP@0.5	AP@0.75	AP_S	AP_M	AP_L
<i>two-stage</i>								
Fast RCNN [3]	VGG16	train	19.7	35.9	-	-	-	-
Faster RCNN [†] [4]	MobileNet	trainval32k	19.8	-	-	-	-	-
Faster RCNN [4]	ResNet101	trainval	29.4	48.0	-	9.0	30.5	47.1
OHEM [27]	VGG16	trainval	22.6	42.5	22.2	5.0	23.7	37.9
ION [26]	VGG16	train+S	23.6	43.2	23.6	6.4	24.1	38.3
OHEM++ [27]	VGG16	trainval	25.5	45.9	26.1	7.4	27.7	40.3
R-FCN [5]	ResNet101	trainval	29.9	51.9	-	10.8	32.8	45.0
Deformable Faster RCNN [36]	ResNet101	trainval	33.1	50.3	-	11.6	34.9	51.2
CoupleNet [23]	ResNet101	trainval	34.4	54.8	37.2	13.4	38.1	50.8
Faster RCNN+++ [44]	ResNet101-c4	trainval	34.9	55.7	37.4	15.6	38.7	50.9
Deformable RFCN [36]	ResNet101	trainval	34.5	55.0	-	14.0	37.7	50.3
Attention CoupleNet [24]	ResNet101	trainval+S	35.4	55.7	37.6	13.2	38.6	52.5
<i>single-stage</i>								
SSD300 [†] [7]	MobileNet	trainval35k	19.3	-	-	-	-	-
RFBNet300 [†] [33]	MobileNet	trainval35k	20.7	-	-	-	-	-
YOLOv2 [31]	Darknet19	trainval35k	21.6	44.0	19.2	5.0	22.4	35.5
SSD300 [7]	VGG16	trainval35k	25.1	43.1	25.8	6.6	25.9	41.4
RON384 [32]	VGG16	train	27.4	49.5	27.1	-	-	-
SSD321 [30]	ResNet101	trainval35k	28.0	45.4	29.3	6.2	28.3	49.3
DSSD321 [30]	ResNet101	trainval35k	28.0	46.1	29.2	7.4	28.1	47.6
SSD512 [7]	VGG16	trainval35k	28.8	48.5	30.3	10.9	31.8	43.5
RefineDet320 [8]	VGG16	trainval35k	29.4	49.2	31.3	10.0	32.0	44.4
RFBNet300 [33]	VGG16	trainval35k	30.3	49.3	31.8	11.8	31.9	45.9
SSD513 [30]	ResNet101	trainval35k	31.2	50.4	33.3	10.2	34.5	49.8
RefineDet512 [8]	VGG16	trainval35k	33.0	54.5	35.5	16.3	36.3	44.3
DSSD513 [30]	ResNet101	trainval35k	33.2	53.3	35.2	13.0	35.4	51.1
RetinaNet500 [29]	ResNet101	trainval35k	34.4	53.1	36.8	14.7	38.5	49.1
RFBNet512 [33]	VGG16	trainval35k	34.4	55.7	36.4	17.6	37.0	47.6
DRN320 [†]	MobileNet	trainval35k	26.0/25.7	45.3	26.8	8.0	28.7	38.9
DRN512 [†]	MobileNet	trainval35k	28.5/28.4	49.8	29.6	14.3	32.1	36.6
DRN320	VGG16	trainval35k	30.5	51.2	32.3	11.2	33.9	44.9
DRN512	VGG16	trainval35k	34.3	57.1	36.4	17.9	38.1	44.8

†: Prior MobileNet-based models are tested on COCO minival2014, so our MobileNet-based AP is reported as “test-dev2015/minival2014”.

and VOC 2012 trainval sets plus VOC 2007 test set (21, 503 images) for training in this experiment, and test models on VOC 2012 test set (10, 991 images). The learning rate schedule is consistent with VOC 2007 training. Referring to Table III, our DRN320 obtains 79.3% mAP that outmatch all compared methods with similar small input size. With 512×512 input size, DRN512 improves the mAP to 80.6%, which validates the effectiveness of our designs once again.

D. Results on COCO

We perform a thorough analysis on COCO detection dataset, which contains 80 class labels. As in previous work, we also use the union of training images and a subset of validation images (118, 278 images, denoted as “trainval35k”) for training, and test models on test-dev2015 set (20, 288k images). The whole network is trained for 70 epochs with a learning rate of 0.001, then for 30 epochs with a learning rate of 0.0001 and another 30 epochs with a learning rate of 0.00001. The main COCO metric denotes as AP, which evaluates detection

results at $\text{IoU} \in [0.5 : 0.05 : 0.95]$. AP@0.5, AP@0.75, and AP_S , AP_M , AP_L (AP at different scales) are also used for deep comparison.

Table IV shows our results. DRN320 achieves the results of 30.5%, which is better than contemporary methods (e.g., RefineDet320, RFBNet300), so our approach can effectively cope with a variety of complex situations with small input resolution. Furthermore, DRN512 obtains a more competitive AP of 34.3%. Because they have similar AP results, we draw readers’ attention to a deep comparison among methods in boldface. At first, DRN512 has huge improvements as opposed to RefineDet512 on all criteria, where our designs are proved to be successful. Moreover, our DRN512 has the best VOC-like AP@0.5 (i.e., 57.1%) and AP_S (i.e., 17.6%), so our method is more adept at small object detection owing to the proposed dual refinement mechanism. However, our results on AP@0.75 and AP_L are not comparable with that of some methods. This is caused by two reasons: i) two-stage methods use larger input size; ii) ResNet101 or RFB block

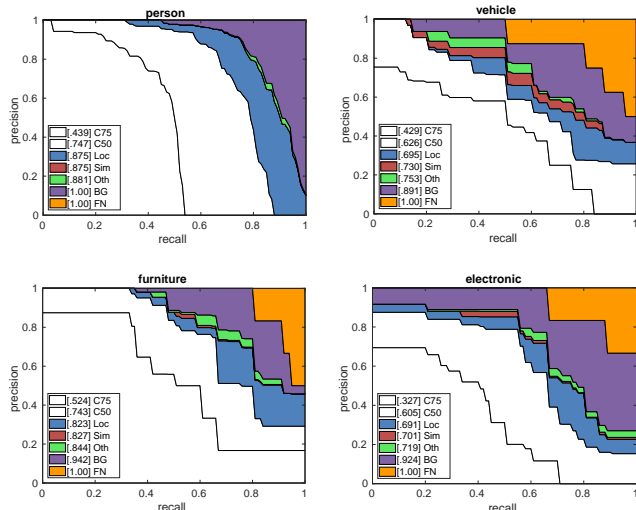


Fig. 8. Error analysis of DRN512 on person, vehicle, furniture, and electronic classes in the COCO 2014 minival set. Each sub-figure shows the cumulative fraction of detections that are correct (Cor) or false positive due to poor localization (Loc), confusion with similar categories (Sim), with others (Oth), or with background (BG).

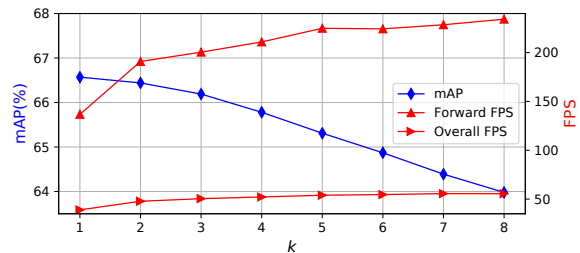
[33] provides larger effective receptive field for describing large objects [45]. Nevertheless, this paper attempts to detect objects at a considerably fast inference speed, but ResNet101-based models can hardly work in real time. Additionally, using MobileNet [42] as the backbone, our DRN outperforms Faster RCNN, SSD, and RFBNet by a substantial margin.

Error analysis of DRN512 is conducted on COCO 2014 minival set (5,000 images), and precision-recall curves are shown on person, vehicle, furniture, and electronic classes. From Fig. 8, it is seen that there exists room for improvement of location precision. As for classification, DRN has less confusion with similar categories or others (Sim & Oth). Thus, our approach is good at inter-class inference, benefiting from accurate single-stage detection features generated by the feature offset refinement. By contrast, the error caused by the background is slightly serious. Probable improvement proposals will be discussed in Section V-F.

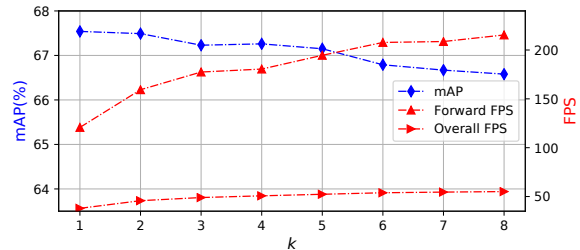
E. Results on ImageNet VID

TRN and TDRN are evaluated on ImageNet VID dataset [9], which requires algorithms to detect 30-class targets in consecutive frames. There are 4000 videos in the training set (1,181,113 frames), and 555 videos in the validation set (176,126 frames). The initial learning rate is 0.001 for the first 70 epochs, then we use a learning rate of 0.0001 for the next 30 epochs and 0.00001 for another 30 epochs. For fast inference speed, all models use 320×320 input images.

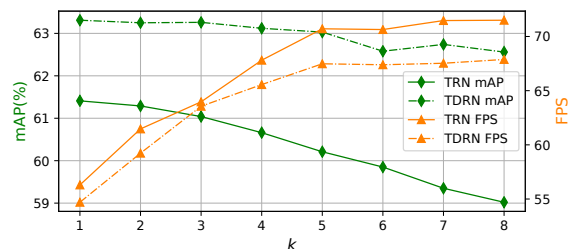
1) *Accuracy vs. Speed Trade-Off on TRN and TDRN*: SSD with 4-scale detection features serves as the baseline (see Fig 5(a)), called SSD4s, and RG and RD are also contrasted with the same structure. As a result, SSD4s-VGG16 and SSD4s-MobileNet obtain 63.0%, 58.3% in mAP, respectively. The key frame duration is used for temporal detection, so accuracy vs. speed trade-off based on k is first analyzed.



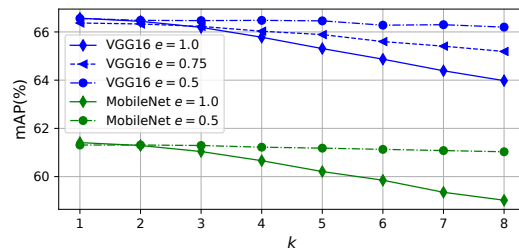
(a) TRN-VGG16. The baseline is 63.0%.



(b) TDRN-VGG16. The baseline is 63.0%.



(c) TRN and TDRN with MobileNet. The baseline is 58.3%.



(d) TRN with VGG16 and MobileNet. e is the loose factor.

Fig. 9. Inference analysis of TRN and TDRN with reference update period k and loose factor e . Note that *Forward FPS* does not consider the time consumption caused by NMS.

As shown in Fig. 9(a), TRN significantly improves the mAP by 3.6% (i.e., 66.6% vs. 63.0). As k increasing, the mAP decreases while the speed raises. Note that NMS impacts detection speed to some extent, but this part is out of the scope of this paper, so the FPS without NMS is also reported (denoted as *Forward FPS*). As plotted in Fig. 9(a), *Forward FPS* increases from 136.8 to 234.2 with the rise of k , and the overall speed can reach 55.5 FPS. Furthermore, TDRN improves the performance up to 67.5% benefiting from the proposed anchor-offset detection, which outperforms the baseline by 4.5 points. When $k = 8$, TDRN can run at 55.1 FPS (*Forward FPS* reaches 215.4) while maintaining the mAP of 66.6%. As for $k = 1, 2, \dots, 8$, TRN has 2.6-point drop in mAP (i.e., 66.6% vs. 64.0%), whereas TDRN only has a mAP decrease of

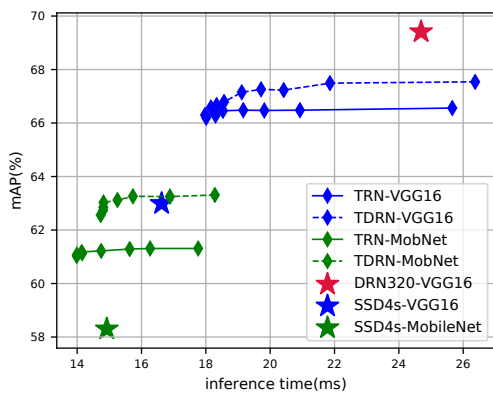


Fig. 10. The plot of mAP vs. inference time for approaches in this paper.

0.9% (i.e., 67.5% vs. 66.6%). Thus, the refinement information in TDRN is more robust in terms of temporal propagation owing to more accurate feature sampling locations generated by our proposed feature offset refinement. Additionally, using MobileNet as the backbone, TRN and TDRN achieve 60.7% and 63.1% mAP ($k = 4$), which surpass the baseline by 2.4 and 4.8 points, respectively. Meanwhile, our MobileNet-based model can run over 70 FPS (Noted that the speed of MobileNet in Pytorch is slightly slower than the official implementation).

To overcome TRN’s rapid mAP decrease with increasing k , the loose refinement strategy is introduced to TRN with a loose factor e . Referring to Fig. 9(d), $e = 0.5$ can restrict this mAP drop within 1% from $k = 1$ to $k = 8$, i.e., 66.6% vs. 66.2% for VGG16 and 61.3% vs. 61.0% for MobileNet.

As shown in Fig. 10, with 320×320 input size, this paper presents a series of approaches for the trade-off between accuracy and speed. The fast solution is TRN-MobileNet ($k = 8$) with a mAP of 61.0% and an inference time of 14 ms. The most accurate method in this paper is DRN320 with 69.4% mAP and 25 ms in inference. In terms of TDRN-VGG16 and DRN320-VGG16, it can be seen that DRN is more accurate owing to FPN structure and multi-deformable head, yet TDRN has a better trade-off between accuracy and speed.

2) *Comparison with Other Architectures*: TRN and TDRN are compared against several prior and contemporary approaches in Table V. Existing video detectors are categorized into offline methods (i.e., batch-frame mode) and online methods. Most methods are based on a two-stage detector and a deep backbone, so they usually have high mAP yet impractical execution time. As for offline approaches, this non-causal batch-frame mode usually leverages both previous and future information that prohibits it from real-world applications. In addition, recent works usually borrow other temporal modules (e.g., tracker, optical flow, and LSTM) to integrate multi-frame information. Among single-stage methods, TDRN-VGG16 has a significant superiority in accuracy, i.e., 1.9% and 12.9% higher mAP than TSSD and LSTM-SSD, respectively. When compared to MobileNet-based detectors, TDRN-MobileNet has the best results, i.e., it outperforms LSTM-SSD by 8.7 points and surpasses HPVD-Mob by 2.9 points. To the best of our knowledge, our designs have the following merits:

TABLE V
Comparison of the proposed methods and several prior and contemporary approaches on VID. $k = 4$ FOR TRN AND TDRN.

Method	Components			Performances	
	Backbone	Flow Tracking	RNN	Real time	mAP(%)
<i>static methods</i>					
SSD4s320	MobileNet			✓	58.3
SSD4s320	VGG16			✓	63.0
Faster RCNN [4]	GoogLeNet				63.0
SSD300 [7]	VGG16			✓	63.0
RefineDet320 [8]	VGG16			✓	66.7
DRN320	VGG16			✓	69.4
<i>offline methods</i>					
STMN [17]	VGG16			✓	55.6
TPN [20]	GoogLeNet			✓	68.4
FGFA [13]	ResNet101	✓			76.3
HPVD [14]	ResNet101	✓			78.6
STSN [16]	ResNet101				78.7
<i>online methods</i>					
LSTM-SSD [18]	MobileNet			✓	54.4
HPVD-Mob [15]	MobileNet	✓		✓	60.2
TCNN [11]	DeepID+Craft	✓	✓		61.5
TSSD [19]	VGG16			✓	65.4
D&T [12]	ResNet101		✓		78.7
TRN	MobileNet			✓	61.2
TDRN	MobileNet			✓	63.1
TRN	VGG16			✓	66.5
TDRN	VGG16			✓	67.3

i) instead of borrowing other temporal modules, temporal information is exploited from the detector itself. Thus, our design is a new online detection mode for videos; ii) TDRN achieves the highest mAP among real-time online temporal detectors, and it induces a better trade-off between accuracy and speed for real-world tasks.

F. Discussion

1) *Key Frame Scheduling*: Zhu *et al.* developed an adaptive key frame scheduling [14] for key frame selection, and we employ a pre-fixed key frame duration. We argue that the adaptive key frame scheduling is needless for both accuracy and speed in this paper: i) any scheduling strategy cannot generate a mAP that outmatches the result of $k = 1$. Therefore, given that the speed of RG is fast enough (i.e., 270 FPS) and a scheduling strategy should deal with each frame, it is better to set $k = 1$ than to use an adaptive key frame scheduling. ii) the longest period is $k = 8$ in our experiments, and we also state that longer detection period is needless: *Forward FPS* of SSD4s-VGG16 is 270 and that of TRN-VGG16 reaches 234 ($k = 8$). Thus, longer key frame duration has an ignorable contribution to inference speed since TRN and TDRN cannot overpass SSD4s in *Forward FPS*.

2) *Further Enhancement of Refinement Networks*: In terms of accuracy, it can be seen from Fig. 8 that there still exists room for improvement of location precision and foreground-background classification. We present two probable solutions: i) multi-step refinement could be beneficial; ii) because of the hard negative mining, only a part of negative samples (i.e.,

background) are used for training. Therefore, using a focal loss [29] to train a network with all negative samples could be more effective. For example, Chi *et al.* used focal loss and negative anchor filtering to train a refinement network and achieved high performance on face detection [46].

Regarding inference speed, the bottleneck is NMS and there could exist two solutions: i) decreasing the anchor amount could be beneficial; ii) an end-to-end detector is becoming urgently necessary. For example, Hu *et al.* developed a relation network for both detection and duplicate removal, so the whole network can perform in an end-to-end manner [47].

G. TDRN-Based Underwater Object Grasping on the Seabed

Underwater missions are quite intractable for humans, so we use an autonomous system for these difficult tasks, i.e., underwater navigation and object grasping. Owing to the characteristic of good accuracy vs. speed trade-off, TDRN is suited to real-world applications. In reality, we employ a remote operated vehicle (ROV) for underwater grasping, where a microcomputer with an Intel I5-6400 CPU, an NVIDIA GTX 1060 GPU, and 8 GB RAM is deployed and a camera is placed in the electric compartment for visual navigation. Based on our proposed method, the ROV is able to approach targets and grasp marine products (e.g., sea cucumbers, sea urchins, and bivalves) using a manipulator. The test venue is located in Zhangzidao, China, where the water depth is approximately 10 m. It should be noted that the training set is from <http://www.cnurpc.org>.

As shown in Fig. 11(a), the ROV works on a natural seabed, and TDRN is competent in detecting objects in an unstructured undersea environment (see Fig. 11(b)). For better visualization, we demonstrate the detection results of sea cucumbers, sea urchins, and bivalves using yellow, cyan, red boxes, respectively. This task is challenging for object detection. On one hand, objects gather together and occlude each other. For example, in the left-bottom of 7th demonstrated frame, a bivalve is almost completely occluded by a sea urchin. On the other hand, many small objects appear in the practical scenario (see the last row of Fig. 11(b)). Despite these difficulties, our proposed TDRN can deal with them efficiently and demonstrate a promising robotic application. The experimental video is available at <https://youtu.be/XDSa4BQX9M8>.

VI. CONCLUSION AND FUTURE WORK

In this paper, we have taken aim at precisely detecting objects in real time for static and temporal scenes. Firstly, drawbacks of the single-stage detector are analyzed from the strengths of two-stage methods. Thereby, a novel anchor-offset detection including an anchor refinement, a feature offset refinement, and a deformable detection head is proposed. Besides two-step regression, the anchor-offset detection is also able to capture accurate single-stage features for detection. Correspondingly, a DRN is proposed based on the anchor-offset detection, where a multi-deformable head is also designed for more contextual information. In the case of temporal detection, we propagate the refinement information in the anchor-offset detection across time and propose a TRN and

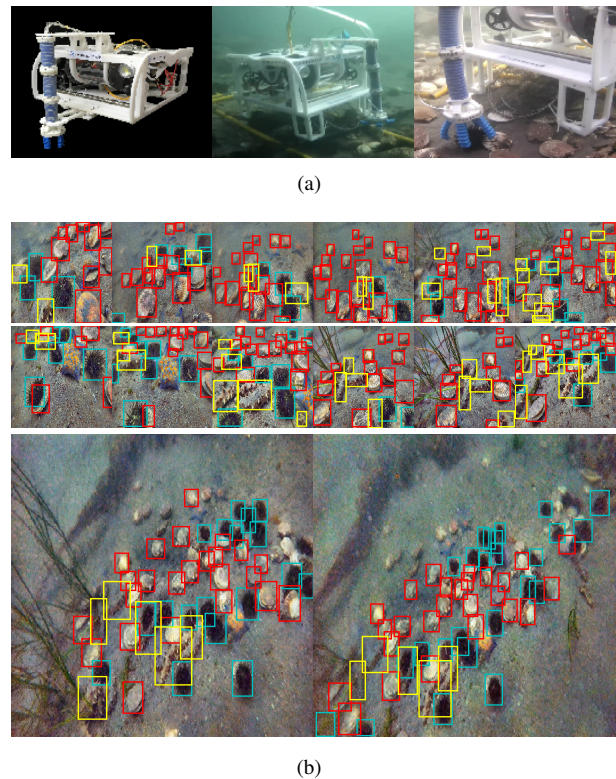


Fig. 11. Schematic examples of an underwater detection task. We use an ROV for underwater grasping. TDRN is trained for detecting seafood animals, i.e., sea cucumbers, sea urchins, and bivalves, which are shown in yellow, cyan, red boxes, respectively. We draw all detected boxes with > 0.4 score. (a) The employed ROV and working scenarios; (b) Detection snapshots.

a TDRN with a reference generator and a refinement detector. Our developed approaches have been evaluated on PASCAL VOC, COCO, and ImageNet VID. As a result, our designs induce a considerably enhanced detection accuracy and see a substantial improvement on the trade-off between accuracy and speed. Finally, the proposed algorithms are applied to underwater object grasping.

In the further, we plan to introduce attention mechanism to the anchor-offset detection and design more effective networks for more robust feature learning. In addition, We will further conduct more real-life missions.

REFERENCES

- [1] Z. Zhao, P. Zheng, S. Xu, and X. Wu, "Object Detection With Deep Learning: A Review," *IEEE Trans. Neural Netw. Learn. Syst.*, doi: 10.1109/TNNLS.2018.2876865
- [2] R. Girshick, J. Donahue, T. Darrell, and J. Malik, "Rich feature hierarchies for accurate object detection and semantic segmentation," in *Proc. IEEE Conf. Comput. Vis. Pattern Recognition*, Columbus, USA, Jun. 2014, pp. 580–587.
- [3] R. Girshick. "Fast R-CNN," in *Proc. IEEE Int. Conf. Comput. Vis.*, Santiago, Chile, Dec. 2015, pp. 1440–1448.
- [4] S. Ren, K. He, R. Girshick, and J. Sun, "Faster R-CNN: Towards real-time object detection with region proposal networks," in *Proc. Adv. Neural Info. Process Syst.*, Montreal, Canada, Dec. 2015, pp. 91–99.
- [5] J. Dai, Y. Li, K. He, and J. Sun, "R-FCN: Object detection via region-based fully convolutional networks," in *Proc. Adv. Neural Info. Process Syst.*, Barcelona, Spain, Dec. 2016, pp. 379–387.
- [6] J. Redmon, S. Divvala, R. Girshick, and A. Farhadi, "You only look once: Unified, real-time object detection," in *Proc. IEEE Conf. Comput. Vis. Pattern Recognition*, Las Vegas, USA, Jun. 2016, pp. 779–788.

- [7] W. Liu, D. Anguelov, D. Erhan, C. Szegedy, S. Reed, C. Y. Fu, and A. C. Berg, "SSD: Single shot multibox detector," in *Proc. Eur. Conf. Comput. Vis.*, Amsterdam, Netherlands, Oct. 2016, pp. 21–37.
- [8] S. Zhang, L. Wen, X. Bian, Z. Lei, S. Z. Li, "Single-shot refinement neural network for object detection," in *Proc. IEEE Conf. Comput. Vis. Pattern Recognition*, Salt Lake City, USA, Jun. 2018, pp. 4203–4212.
- [9] O. Russakovsky, J. Deng, H. Su, J. Krause, S. Satheesh, S. Ma, Z. Huang, A. Karpathy, A. Khosla, M. Bernstein, A. C. Berg, and F. Li, "ImageNet large scale visual recognition challenge," *Int. J. Comput. Vis.*, vol. 115, no. 3, pp. 211–252, 2015.
- [10] W. Han, P. Khorrani, T. L. Paine, P. Ramachandran, M. Babaeizadeh, H. Shi, J. Li, S. Yan, and T. S. Huang, "Seq-NMS for video object detection," *arXiv:1602.08465*, 2016.
- [11] K. Kang, H. Li, J. Yan, X. Zeng, B. Yang, T. Xiao, C. Zhang, Z. Wang, R. Wang, X. Wang, and W. Ouyang, "T-CNN: Tubelets with convolutional neural networks for object detection from videos," *IEEE Trans. Circuits Syst. Video Technol.*, DOI: 10.1109/TCSVT.2017.2736553.
- [12] C. Feichtenhofer, A. Pinz, and A. Zisserman, "Detect to track and track to detect," in *Proc. Int. Conf. Comput. Vis.*, Venice, Italy, Oct. 2017, pp. 3038–3046.
- [13] X. Zhu, Y. Wang, J. Dai, L. Yuan, and Y. Wei, "Flow-guided feature aggregation for video object detection," in *Proc. Int. Conf. Comput. Vis.*, Venice, Italy, Oct. 2017, pp. 408–417.
- [14] X. Zhu, J. Dai, L. Yuan, and Y. Wei, "Towards high performance video object detection," in *Proc. IEEE Conf. Comput. Vis. Pattern Recognition*, Salt Lake City, USA, Jun. 2018, pp. 7210–7218.
- [15] X. Zhu, J. Dai, X. Zhu, Y. Wei, and L. Yuan, "Towards high performance video object detection for mobiles," *arXiv:1804.05830*, 2018.
- [16] G. Bertasius, L. Torresani, and J. Shi, "Object detection in video with spatiotemporal sampling networks," in *Proc. Eur. Conf. Comput. Vis.*, Munich, Germany, Sept. 2018, pp. 342–357.
- [17] F. Xiao and Y. J. Lee, "Video object detection with an aligned spatial-temporal memory," in *Proc. Eur. Conf. Comput. Vis.*, Munich, Germany, Sept. 2018, pp. 494–510.
- [18] M. Liu and M. Zhu, "Mobile video object detection with temporally-aware feature maps," in *Proc. IEEE Conf. Comput. Vis. Pattern Recognition*, Salt Lake City, USA, Jun. 2018, pp. 5686–5695.
- [19] X. Chen, J. Yu, and Z. Wu, "Temporally Identity-Aware SSD with Attentional LSTM," *IEEE Trans. Cybern.*, to be published, doi:10.1109/TCYB.2019.2894261.
- [20] K. Kang H. Li, T. Xiao, W. Ouyang, J. Yan, X. Liu, and X. Wang, "Object detection in videos with tubelet proposal networks," in *Proc. IEEE Conf. Comput. Vis. Pattern Recognition*, Hawaii, USA, Jul. 2017, pp. 727–735.
- [21] M. Everingham, L. Van Gool, C. K. Williams, J. Winn, and A. Zisserman, "The pascal visual object classes (voc) challenge," *Int. J. Comput. Vis.*, vol. 88, no. 2, pp. 303–338, 2010.
- [22] T. Y. Lin, M. Maire, S. Belongie, J. Hays, P. Perona, D. Ramanan, P. Dollar, and C. L. Zitnick, "Microsoft coco: Common objects in context," in *Proc. Eur. Conf. Comput. Vis.*, Zurich, Switzerland, Sept. 2014, pp. 740–755, 2014.
- [23] Y. Zhu, C. Zhao, J. Wang, X. Zhao, Y. Wu, H. Lu, "Couplenet: Coupling global structure with local parts for object detection," in *Proc. IEEE Int. Conf. Comput. Vis.*, Venice, Italy, Aug. 2017, pp. 4126–4134.
- [24] Y. Zhu, C. Zhao, H. Guo, J. Wang, X. Zhao, and H. Lu, "Attention couplenet: Fully convolutional attention coupling network for object detection," *IEEE Trans. Image Process.*, vol. 28, no. 1, pp. 113–126, 2019.
- [25] T. Kong, A. Yao, Y. Chen, and F. Sun, "Hypernet: Towards accurate region proposal generation and joint object detection," in *Proc. IEEE Conf. Comput. Vis. Pattern Recognition*, Las Vegas, USA, Jun. 2016, pp. 845–853.
- [26] S. Bell, C. L. Zitnick, K. Bala, and R. B. Girshick, "Insideoutside net: Detecting objects in context with skip pooling and recurrent neural networks," in *Proc. IEEE Conf. Comput. Vis. Pattern Recognition*, Las Vegas, USA, Jun. 2016, pp. 2874–2883.
- [27] A. Shrivastava, A. Gupta, and R. B. Girshick, "Training region-based object detectors with online hard example mining," in *Proc. IEEE Conf. Comput. Vis. Pattern Recognition*, Las Vegas, USA, Jun. 2016, pp. 761–769.
- [28] T. Y. Lin, P. Dollar, R. Girshick, K. He, B. Hariharan, and S. Belongie, "Feature pyramid networks for object detection," in *Proc. IEEE Conf. Comput. Vis. Pattern Recognition*, Hawaii, USA, Jun. 2017, pp. 2117–2125.
- [29] T. Y. Lin, P. Goyal, R. Girshick, K. He, and P. Dollar, "Focal loss for dense object detection," in *Proc. IEEE Int. Conf. Comput. Vis.*, Venice, Italy, Oct. 2017, pp. 2980–2988.
- [30] C. Fu, W. Liu, A. Ranga, A. Tyagi, and A. C. Berg, "DSSD: Deconvolutional single shot detector," *arXiv:1701.06659*, 2017.
- [31] J. Redmon and A. Farhadi, "YOLO9000: Better, faster, stronger," in *Proc. IEEE Conf. Comput. Vis. Pattern Recognition*, Hawaii, USA, Jul. 2017, pp. 6517–6525.
- [32] T. Kong, F. Sun, A. Yao, H. Liu, M. Lu, and Y. Chen, "RON: Reverse connection with objectness prior networks for object detection," in *Proc. IEEE Conf. Comput. Vis. Pattern Recognition*, Hawaii, USA, Jun. 2017, pp. 5936–5944.
- [33] S. Liu, D. Huang, and Y. Wang, "Receptive field block net for accurate and fast object detection," in *Proc. Eur. Conf. Comput. Vis.*, Munich, Germany, Sept. 2018, pp. 404–419.
- [34] Z. Shen, Z. Liu, J. Li, Y. Jiang, Y. Chen, and X. Xue, "DSOD: Learning deeply supervised object detectors from scratch," in *Proc. IEEE Int. Conf. Comput. Vis.*, Venice, Italy, Oct. 2017, pp. 1919–1927.
- [35] Y. Pang, J. Cao, and X. Li, "Learning sampling distributions for efficient object detection," *IEEE Trans. Cybern.*, vol. 47, no. 1, pp. 117–129, 2017.
- [36] J. Dai H. Qi, Y. Xiong, Y. Li, G. Zhang, H. Hu, and Y. Wei, "Deformable Convolutional Networks," in *Proc. Int. Conf. Comput. Vis.*, Venice, Italy, Oct. 2017, pp.764–773.
- [37] X. Glorot and Y. Bengio, "Understanding the difficulty of training deep feedforward neural networks," in *Proc. Int. Conf. Artificial Intell. Statist.*, Sardinia, Italy, May 2010, pp. 249–256.
- [38] S. Ioffe, and C. Szegedy, "Batch normalization: Accelerating deep network training by reducing internal covariate shift," in *Proc. Int. Conf. Machine Learn.*, Lille, France, Jul. 2015, pp. 448–456.
- [39] K. Simonyan and A. Zisserman, "Very deep convolutional networks for large-scale image recognition," *arXiv:1409.1556*, 2014.
- [40] C. Szegedy, W. Liu, Y. Jia, P. Sermanet, S. Reed, D. Anguelov, D. Erhan, V. Vanhoucke, and A. Rabinovich, "Going deeper with convolutions," in *Proc. IEEE Conf. Comput. Vis. Pattern Recognition*, Boston, USA, Jun. 2015, pp. 1–9.
- [41] K. He, X. Zhang, S. Ren, and J. Sun, "Deep residual learning for image recognition," in *Proc. IEEE Conf. Comput. Vis. Pattern Recognition*, Las Vegas, USA, Jun. 2016, pp. 770–778.
- [42] A. Howard, M. Zhu, B. Chen, D. Kalenichenko, W. Wang, T. Weyand, M. Andreetto, and H. Adam, "Mobilenets: Efficient convolutional neural networks for mobile vision applications," *arXiv:1704.04861*, 2017.
- [43] G. Huang, Z. Liu, K. Q. Weinberger, and L. van der Maaten, "Densely connected convolutional networks," in *Proc. IEEE Conf. Comput. Vis. Pattern Recognition*, Hawaii, USA, Jun. 2017, pp. 4700–4708.
- [44] K. He, X. Zhang, S. Ren, and J. Sun, "Deep residual learning for image recognition," in *Proc. IEEE Conf. Comput. Vis. Pattern Recognition*, Las Vegas, USA, Jun. 2016, pp. 770C778.
- [45] W. Luo, Y. Li, R. Urtasun, and R. Zemel, "Understanding the effective receptive field in deep convolutional neural networks," in *Proc. Adv. Neural Info. Process. Syst.*, Barcelona, Spain, Dec. 2016, pp. 4898–4906.
- [46] C. Chi, S. Zhang, S. Xing, J. Lei, S. Z. Li, and X. Zou, "Selective refinement network for high performance face detection," *arXiv:1809.02693*, 2018.
- [47] H. Hu, J. Gu, Z. Zhang, J. Dai, Y. Wei, "Relation networks for object detection," in *Proc. IEEE Conf. Comput. Vis. Pattern Recognition*, Salt Lake City, USA, Jun. 2018, pp. 3588–3597.

TABLE VI
AP LIST ON PASCAL VOC TEST SET BY THE PROPOSED METHODS. ALL MODELS USE VGG16 AS THE BACKBONE NETWORK.

Method	aero	bike	bird	boat	bottle	bus	car	cat	chair	cow	table	dog	horse	mbike	person	plant	sheep	sofa	train	tv	mAP
<i>VOC 2007</i>																					
DRN320	86.31	87.45	83.01	77.35	66.12	87.95	88.64	89.44	69.30	85.73	76.34	87.50	88.99	87.16	83.94	57.48	85.24	82.28	88.07	82.12	82.02
DRN512	88.83	86.52	85.45	77.50	72.23	88.05	89.03	89.92	68.58	88.11	76.81	87.50	89.30	85.50	85.44	59.18	85.95	80.75	87.30	82.99	82.75
<i>VOC 2012</i>																					
DRN320	88.92	87.12	80.36	69.18	60.23	84.49	82.77	92.42	62.27	83.33	66.76	91.08	88.01	87.21	86.79	57.79	82.97	72.09	88.04	75.07	79.34
DRN512	91.57	88.00	83.27	69.42	68.45	85.53	85.53	93.16	62.10	85.51	65.40	91.69	87.89	88.51	88.56	59.68	86.68	66.64	88.98	75.83	80.60

TABLE VII
OBJECT DETECTION RESULTS ON THE MS COCO 2015 TEST-DEV SET.

Method	AP	AP@0.5	AP@0.75	AP _S	AP _M	AP _L	AR ₁	AR ₁₀	AR ₁₀₀	AR _S	AR _M	AR _L
DRN320-MobileNet	26.0	45.3	26.8	8.0	28.7	38.9	24.1	36.4	38.4	13.0	44.2	56.9
DRN512-MobileNet	28.5	49.8	29.6	14.3	32.1	36.6	25.5	39.9	42.2	22.2	47.3	55.0
DRN320-VGG16	30.5	51.2	32.3	11.2	33.9	44.9	27.0	40.9	42.9	17.5	49.0	62.2
DRN512-VGG16	34.3	57.1	36.4	17.9	38.1	44.8	28.9	44.8	47.4	26.6	52.7	61.5

TABLE VIII
AP LIST ON IMAGENET VID 2017 VALIDATION SET BY THE PROPOSED METHODS. ALL MODELS USE 320×320 INPUT IMAGES AND ARE TRAINED WITH VID+DET DATASET. $k = 4$ IN TRN AND TDRN INFERENCE.

Method	airplane	antelope	bear	bicycle	bird	bus	car	cattle	dog	d.cat	elephant	fox	g.panda	hamster	horse	lion
DRN320	87.56	80.96	71.18	69.63	69.25	68.53	64.12	73.03	55.93	65.48	73.73	85.63	81.84	89.78	69.86	34.89
SSD4s-VGG16	83.45	71.62	66.16	57.23	63.02	73.13	58.79	58.05	54.88	66.39	70.56	79.30	80.67	86.00	64.50	38.52
TRN-VGG16	83.38	69.42	71.54	60.44	63.93	69.74	58.67	58.64	54.84	71.60	69.96	84.79	81.15	89.28	69.33	39.72
TDRN-VGG16	83.67	73.80	71.48	60.89	64.09	75.22	59.94	60.81	57.49	70.59	71.39	84.55	81.93	88.47	68.42	46.49
SSD4s-MobileNet	81.35	71.27	67.15	52.10	59.28	66.15	58.23	54.87	46.35	61.61	65.50	73.79	79.50	75.12	59.36	9.19
TRN-MobileNet	80.87	72.99	67.23	56.10	62.54	68.61	59.46	61.16	48.77	62.51	67.34	72.43	78.94	83.54	65.54	15.54
TDRN-MobileNet	82.67	76.91	62.92	58.67	63.97	69.10	59.91	61.50	53.17	67.55	65.98	74.74	80.77	85.29	65.55	11.89
Method	lizard	monkey	m.bike	rabbit	r.panda	sheep	snake	squirrel	tiger	train	turtle	w.craft	whale	zebra	mAP	
DRN320	71.40	43.20	80.79	52.99	62.35	60.56	52.63	47.76	89.16	82.82	76.24	62.03	69.81	89.24	69.41	
SSD4s-VGG16	60.56	40.76	75.68	45.47	16.77	48.88	44.48	46.14	84.27	76.26	70.46	66.23	57.43	83.95	62.99	
TRN-VGG16	69.31	42.58	76.78	53.03	55.05	51.35	53.36	47.61	86.34	78.55	73.31	62.25	63.11	85.50	66.49	
TDRN-VGG16	72.63	42.36	77.43	56.59	41.32	58.49	45.75	50.82	85.16	81.13	74.36	62.30	65.53	84.82	67.26	
SSD4s-MobileNet	54.17	33.51	72.19	41.43	21.81	51.51	35.60	41.47	83.72	75.54	63.05	53.73	57.53	82.81	58.30	
TRN-MobileNet	55.25	36.65	73.87	55.19	29.41	52.22	40.69	44.88	83.61	73.71	69.78	53.54	59.93	84.55	61.23	
TDRN-MobileNet	58.36	37.54	77.13	58.39	49.43	50.24	35.56	45.05	84.07	77.45	71.97	59.74	63.85	84.42	63.13	

SUPPLEMENT: COMPLETE OBJECT DETECTION RESULTS set are shown in Tables VI, VII, and VIII.

The complete object detection results of the proposed methods on PASCAL VOC, COCO and ImageNet VID validation